Critical Discussion of Ex situ and In situ TEM Measurements on Memristive Devices

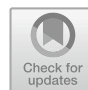

Ole Gronenberg, Georg Haberfehlner, Finn Zahari, Richard Marquardt, Christian Kübel, Gerald Kothleitner, and Lorenz Kienle

Abstract Memristors are promising candidates for new memory technologies and are capable to mimic synapses in artificial neural networks. The switching in memristive devices occurs typically in few nanometer thin dielectric layers. The direct observation of the switching mechanism is crucial for better comprehension and improvements of memristors. Therefore, in situ experiments are conducted in a transmission electron microscope (TEM). However, sample preparation processes and electron beam irradiation can lead to a chemical and structural modification of the active layers. Moreover, devices may show significant device-to-device variability due to the details of processing parameters. Thus, it is essential to characterize the identical device electrically before microstructural analysis.

O. Gronenberg · L. Kienle (✉)
Synthesis and Real Structure, Department of Materials Science, Kiel University, Kaiserstr. 2, 24143 Kiel, Germany
e-mail: lk@tf.uni-kiel.de

O. Gronenberg
e-mail: og@tf.uni-kiel.de

G. Haberfehlner · G. Kothleitner
Institute for Electron Microscopy and Nanoanalytics, Technical University Graz, Steyrergasse 17, 8010 Graz, Austria
e-mail: georg.haberfehlner@felmi-zfe.at

G. Kothleitner
e-mail: gerald.kothleitner@felmi-zfe.at

F. Zahari · R. Marquardt
Nanoelectronics, Department of Electrical Engineering and Information Engineering, Kiel University, Kaiserstr. 2, 24143 Kiel, Germany
e-mail: fnz@tf.uni-kiel.de

R. Marquardt
e-mail: rvm@tf.uni-kiel.de

C. Kübel
Institute of Nanotechnology, Karlsruhe Institute of Technology, 76344 Eggenstein-Leopoldshafen, Germany
e-mail: christian.kuebel@kit.edu

© The Author(s) 2024

M. Ziegler et al. (eds.), *Bio-Inspired Information Pathways*, Springer Series on Bio- and Neurosystems 16, https://doi.org/10.1007/978-3-031-36705-2_5

1 Introduction

Is Moore's Law at an end? Memrisitve devices can help to extend the functionality of today's state-of-the art digital computers while simultaneously decrease energy consumption for data intensive and associative tasks in novel in-memory and bio-inspired computing architectures [1, 2]. The usual two-terminal device structure can further help to decrease the size of integrated circuits and memory arrays.

Simple two-terminal memristive devices can help to further decrease the feature size in integrated circuits, while simultaneously decreasing energy consumption. However, with decreasing feature size, every single structural and electronic defect becomes more important and analytical techniques become the limiting factor for knowledge-driven engineering of memristive devices. In this chapter, the limits of TEM are critically discussed. TEM, as one of the suitable analytical methods, provides sufficient resolution as well as a plethora of different techniques to obtain information from real space, reciprocal space and spectroscopy. Recent progress in TEM analysis of memristive devices is reviewed in publications of Strobel et al. [3], Yang et al. [4], Sun et al. [5], Xu et al. [6] and Yang et al. [7].

The final goal of most TEM studies on memristive devices is to identify the switching mechanism by directly observing structural or chemical changes or inhomogeneities inside the memristive material. However, the identification of fingerprints for memristive switching is not straightforward as discussed below.

The most studied switching mechanism is the growth and rupture of a conducting filament which is believed to be essential for the electrochemical metalization mechanism (ECM) and in valence change memories (VCMs) [8]. In memristive devices based on the ECM, a metallic filament forms due to the partial dissolution of an active electrode (typically Ag or Cu) into a dielectric layer in high electric fields. Such metallic filaments were often observed in situ in TEM experiments, as summarized in the review from Yang et al. [4]. However, radiolysis and developing electric fields in the sample due to the electron beam complicate such experiments and can lead to unambiguous interpretations. Especially for the thin TEM samples, surface-migration and surface oxidation should be prevented to reduce effects from radiolysis and electric fields.

One of the main defects discussed for resistive switching in the field of VCMs are oxygen vacancies, which are reported to be responsible for the formation of one or multiple conducting filaments inside the dielectric matrix [9]. These vacancies, however, are generally difficult to detect. In the case of TiO_2 memristors, such filaments could be identified by small crystallized regions with decreased oxygen content in the so called Magnéli phases [10]. These can be directly identified by diffraction and imaging techniques in the TEM. In other oxides, however, such direct fingerprints for the filaments are under debate and thus indications are used to identify the filaments, e.g., by spectroscopic means. Li et al. [11] and Jang et al. [12] observed such an indication for HfO_2 in the low loss electron energy loss spectrum (EELS): A plasmon peak change under in situ biasing was interpreted as the change of oxy-

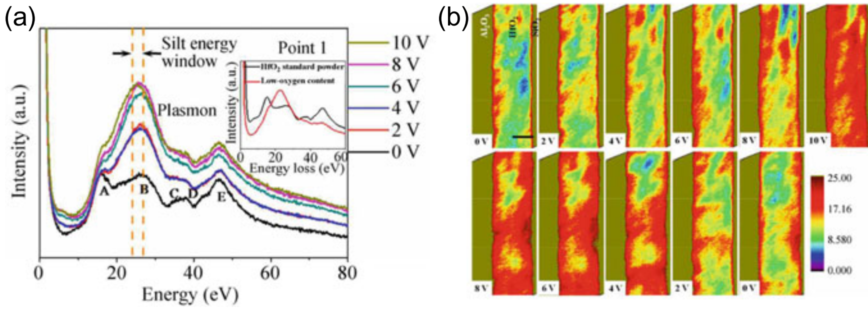

Fig. 1 **a** Low-loss EEL spectra with bias voltages from 0 to 10 V. The slit energy window for the energy filtered (EF)TEM images in **b** is indicated by orange dashed lines. The color code indicates higher oxygen vacancy concentrations. Adapted by permission from [Springer Nature Customer Service Centre GmbH]: [Springer] [Nano Research] [11]

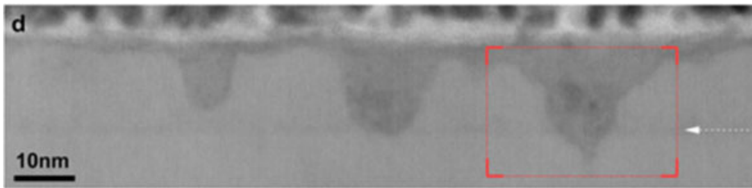

Fig. 2 Annular bright field STEM image of a Au/Fe:$SrTiO_3$/Nb:$SrTiO_3$ memory device after electroforming and delamination of the Au top electrode. Adapted with permission from [ACS Publications][Chemistry of Materials] [9]

gen vacancy concentration and distribution, which could then be mapped in energy filtered (EF)TEM images (see Fig. 1b).

An additional difficulty is presented by the fact, that conducting filaments can be formed anywhere in the memristive device, while TEM can only analyze a limited region of interest. Yang et al. circumvent this problem by electrically probing a HfO_2 thin film with conductive-AFM and fabricating FIB lamellas from probed regions [4]. Such a filament was subsequently observed by means of scanning TEM (STEM) energy dispersive X-ray spectroscopy (EDX) elemental mapping, as it exhibited a reduced oxygen signal. Du et al. delaminated the top electrode of a device after cycling and prepared FIB-lamellas from regions where they detected defects [9]. The observed Ti^{3+} ions indicated oxygen vacancies in $SrTiO_3$ which could be identified by X-ray absorption spectroscopy and X-ray photoemission electron microscopy. Consequently, the researchers were able to show that multiple filaments can be formed simultaneously, but with different velocities (see Fig. 2) [9]. Accordingly to this, an observed filament can be in any resistive state, since a different filament might dominate the resistive switching. Nevertheless, observing and characterizing the filaments present great opportunities to gain a fundamental understanding of switching mechanisms and towards knowledge-based improvements of memristive devices.

However, such experimental results impose a high margin of error since artefacts could be introduced by TEM sample preparation and by beam damage during measurements. Accordingly, great effort should be made to rule out or minimize artifacts. Therefore, the following chapter presents means to achieve suitably pure samples, as well as aspects of best practice. These include TEM sample preparation and the possible induction of artifacts, performing TEM measurements without beam damage and ultimately dedicated *in operando* methods.

2 TEM Sample Preparation

TEM measurements require a specimen thickness below 100 nm and for reliable (electron energy loss) spectroscopic information the thickness should be below 50 nm. This requirement makes the preparation equally important as the experiment and the analysis itself, because unwanted alterations of the material or the device are to be avoided. When analyzing memristive devices, electrical characterization prior to preparation and structural characterization via TEM is crucial and should be carried out on the same device that is to be measured. Memristive devices generally exhibit a high variability from device to device, which complicates the subsequent analysis. Even devices on the same wafer can differ strongly, depending on their position on the wafer. These differences could be attributed to local variances in plasma conditions during sputter-deposition, which result in different oxidation states of the metal oxide components on the wafer, which was proven by EELS fingerprinting of the O-K edge in this case of a niobium oxide thin film [13]. Challenges of preparations of specific devices are summarized below.

2.1 FIB Preparation of Specific Devices

The preparation of cross-sections of single devices on a lithographically structured wafer relies on Focused Ion Beam (FIB) milling with Ga ions combined with scanning electron microscopy to select a specific region of interest. The FIB method enables the preparation of a cross-sectional lamella, a few µm in size, with a homogeneous thickness for high quality measurements. Prior to the Ga ion milling, a protective Pt-layer is deposited with a gas injection source (GIS) that reduces both charging and Ga-implantation in the device. In case of insulating specimens, this Pt-layer might be insufficient as strong charging hinders the Pt-deposition itself. In case of sapphire substrates, electron and Ga ion bombardment can lead to an amorphization of the surface (see. Fig. 3). An alternative preparation method would be using the precision ion polishing system (PIPS), which is described further below. However, due to the method requiring steps of mechanical grinding and thinning steps, preparation proved

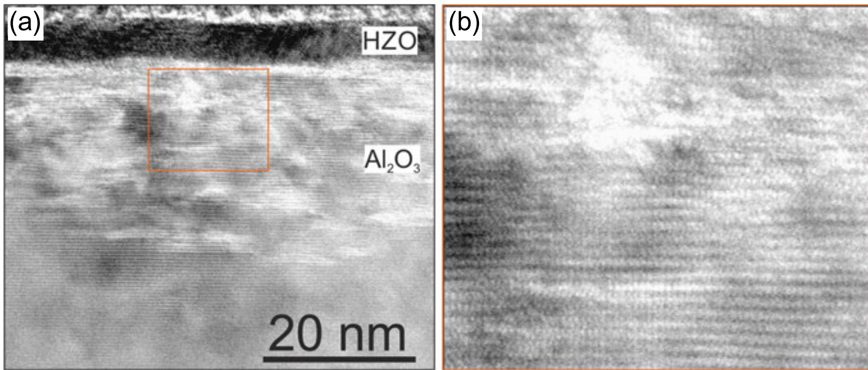

Fig. 3 **a** HRTEM micrograph of hafnium zirconium oxide (HZO) grown on sapphire substrate, prepared as a FIB cross-section. A high defect density is visible at the surface of the substrate. The orange rectangle indicates the magnified region in **b**

to be impossible, as sapphire is one of the hardest materials. In the case of memristive devices, the top electrode protects the underlying layers and reduces charging effects during the FIB preparation.

Independent from the charging effects in the FIB, (e.g., by a sputtered top electrode) dedicated TEM measurements require a final thinning step of the FIB lamella. This can be done in the FIB with Ga ions accelerated with lower voltage from the top of the cross-section. However, this procedure is prone to Ga implantation and surface amorphization.

An alternative approach is to perform the final thinning with Ar ions with low voltages to gently sputter material from the FIB lamella. However, for sapphire substrates, low-energy milling is required, as it has been observed that sapphire is sensitive to Ar ion milling at energies above 3 keV [14]. Sapphire becomes susceptible to electron beam damage in the TEM, which could be prevented when milling specimens with Ar ions with acceleration voltages of 2.5 keV or less [14]. This can be explained by the incorporated Ar point defects that act as nucleation centers for the reduction of Al_2O_3 in the electron beam [15]. Accordingly, oxides, especially with high defect concentrations, should be Ar-milled only if necessary and with low accelerating voltages (e.g., 500 eV) to prevent the creation of defects in the preparation.

Different milling rates along the lamella in the FIB might occur in cases, where the top most layer is inhomogeneous or structured with different materials (e.g., with top electrodes or dielectrics). In these cases it might be helpful to flip the lamella by 180° and to perform the FIB thinning from the backside, i.e., the side of the substrate [16]. Particularly for the most common substrate in many fields, a crystalline Si wafer, this procedure enhances the homogeneity of the FIB lamella. Still, a slightly misoriented Si substrate can result in strong anisotropic etching from different etching rates of different crystal orientations, as can be seen in Fig. 4a, while in Fig. 4b homogeneous

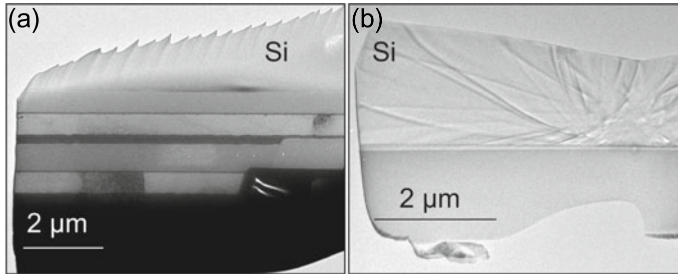

Fig. 4 Two FIB lamellas prepared with a backside thinning procedure, developed in-house, using a rotation tip. In **a**, the lamella was slightly tilted due to stress during transfer to the rotation holder for the 180° rotation. As a result, a saw tooth structure developed due to anisotropic etching in the crystalline Si substrate. In contrast, the lamella in **b** was perfectly aligned for backside thinning resulting in a smooth Si surface

milling was achieved. In Fig. 4a, the FIB lamella was lifted out and attached to a rotation tip for the 180° rotation. During this transfer, the lamella was slightly tilted by stress, leading to a sawtooth structure due to anisotropic etching of the crystalline Si substrate.

In cases where it is suspected that the preparation has produced artifacts, a reference sample must be prepared with a well-established and more sensitive preparation method. Such a method could be using the PIPS at low voltages, which mills a hole inside the sample with Ar ion impact at an oblique angle. With the PIPS, no specific devices can be selected as TEM specimens, though high-quality specimens can be produced. A comparison between FIB and PIPS preparation, acting as check of reliability, has been carried out by the analysis of low-temperature superconducting Josephson junctions as a reference system [17]. Figure 5a exemplifies the slightly different outcome of these procedures: the sample prepared with FIB shows lower contrast and resolution than the sample prepared via PIPS because of higher thickness and some FIB induced amorphization of the surface layers [18]. Importantly, though, the STEM-EDX scan (Fig. 5b) across the layers yielded qualitatively the same result for both cases, showcasing the partial oxidation of the Al layer on the side facing the surface. Since the results show such congruence, the preparation by FIB - which is necessary for the actual devices - is deemed suitable [19].

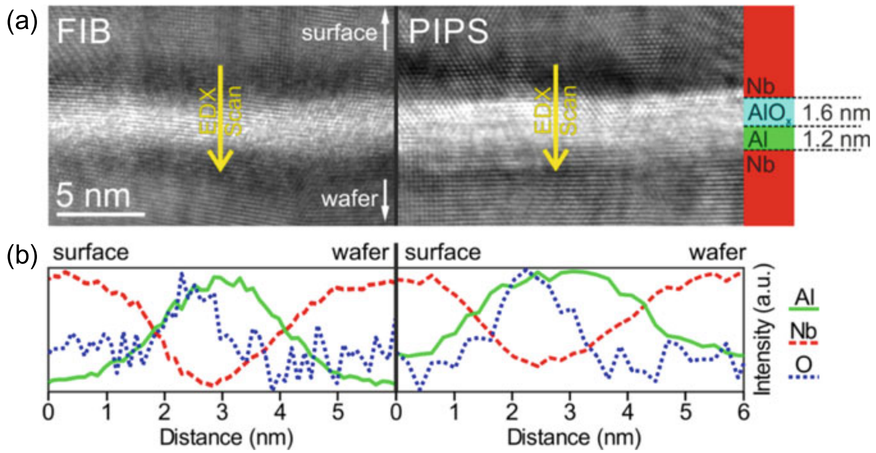

Fig. 5 Comparison of a Josephson junction prepared via FIB (left) and PIPS (right). In **a**, HRTEM shows the polycrystalline nature of the Nb top and bottom electrodes as well as the partially amorphous Al/AlO$_x$ layer in between. The EDX scans in **b**, performed along the yellow arrows in **a**, show both that Al is partially oxidized on the side facing the surface. Adapted with permission of AIP Publishing [19]

2.2 Conclusion for the Preparation

- Protect the topmost layer before preparation to prevent Ga implantation and related artefacts
- Use sensitive preparation methods with low acceleration voltages
- Check for preparation artefacts in the beginning, before starting sophisticated and time-consuming measurements
- If preparation artefacts are likely, compare the same or a well-comparable sample prepared with a more sensitive method (e.g., PIPS)
- Best practice: if possible fabricate a (prototype) device on a TEM-compatible grid to check functionality before, after, or even during measurements.

3 Spectroscopic Methods

Modern TEMs are equipped with EDX spectrometers as standard, since characteristic X-rays are readily formed when the electron beam passes through the sample. These X-rays can be used to determine and even quantify the elements in respect to their concentrations in the sample. Not only the primary beam generates X-rays, but also secondary electrons that interact inside the microscope column and generate spurious X-ray signals. These spurious X-rays, as well as further artifacts and pitfalls, will be discussed in the following chapter.

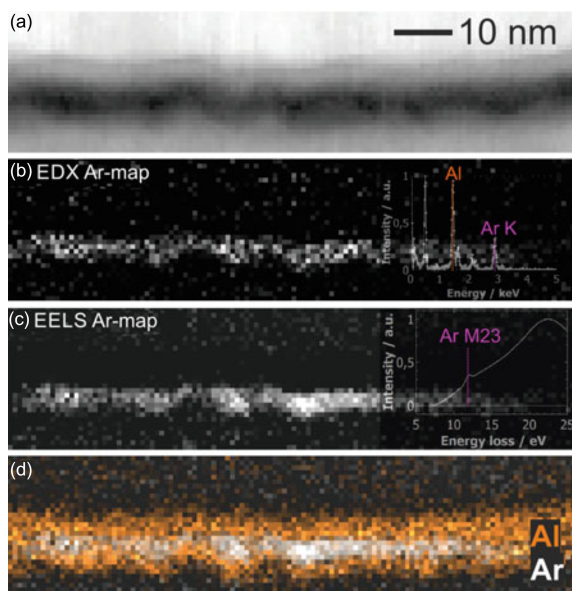

Fig. 6 **a** STEM high angle annular dark field (HAADF) image showing the thin film stack of a DBMD build up from bottom to top of Nb, Al_2O_3, HfO_2 and Au. The spectrum image in **b** is created from the Ar EDX signal and in **c** from the Ar M_{23} EELS signal. The inset in **c** shows the EEL spectrum with the Al_2O_3 plasmon and the sharp M_{23} threshold peak of Ar at 12 eV. The overlayed image in **d** shows the Al EDX signal in orange and the Ar EELS map of **c**

Spurious X-rays are characteristics of the respective microscope and TEM grid in use. Reference spectra next to the sample give a clear indication of which signal is spurious or intrinsic. This procedure fails when the TEM grid contains elements which are also present in the actual specimen. Accordingly, the right TEM grid needs to be chosen beforehand. Further limiting this choice are overlapping EDX peaks between TEM grid and elements that are expected to be in the sample. For instance, peaks of Si and Mo or Ti and Ba overlap and cannot be distinguished with the energy resolution of common EDX detectors.

Artificial peaks can also occur and are produced as sum-peaks when two characteristic X-rays are detected within the processing time of a signal. These sum-peaks can usually be ignored but become critical when an element at the same energy is falsely detected. One prominent example is the sum-peak of Al, which lies at the same position as Ar [20] and could lead to the wrong exclusion of Ar in Al. In a study of a double barrier memristive device (DBMD) including a roughly 7 nm thin Al_2O_3 layer (compare Sect. 4 dealing with this device), an Ar EDX signal was measured exactly in the middle of this layer as shown in Fig. 6b. In this case, an Al sum-peak could be ruled out by the complementary technique EELS. The Ar M_{23} edge at 12 eV (see inset in Fig. 6c) and the L_{23} edge at 320 eV prove the presence of Ar in the Al_2O_3 thin film, which is also indicated by the EDX signal. The EEL spectral image exhibits a significantly better signal-to-noise ratio at the same acquisition time in comparison to the EDX map. The compound map in Fig. 6d of Al (EDX signal) and Ar (EELS signal) shows a clear anti-correlation, suggesting Ar segregation in less dense regions inside the Al_2O_3. Dark contrast in the STEM-HAADF image in Fig. 6c supports this hypothesis.

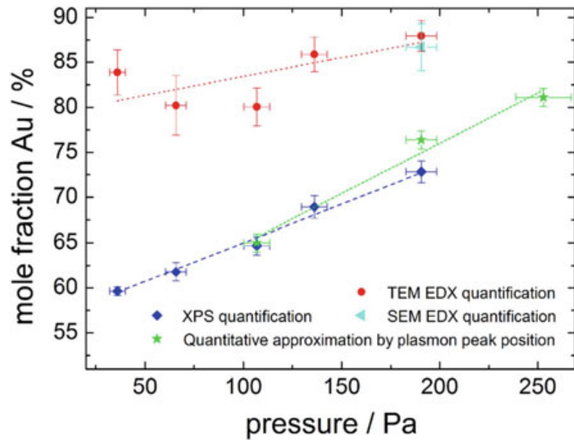

Fig. 7 Mole fraction of Au in AgAu bimetallic nanoparticles deposited with a Haberland type GAS at different Ar pressures. The mole fractions were determined by XPS (blue squares), TEM-EDX (red circles), SEM-EDX (cyan triangle) and approximated from UV–vis spectra (green stars). Adapted with permission from IOP Publishing [21]

The usage of complementary techniques can not only support the measurements but also point the way to further conclusions. As an example, a combination of EDX, X-ray photoelectron spectroscopy (XPS) as well as UV-vis spectroscopy was used to investigate a system of bimetallic nanoparticles. These nanoparticles were fabricated via a custom-made multi-component (e.g., AgAu) target in a Haberland-type gas aggregation cluster source (GAS) and subsequently studied. Since XPS and the optical behavior of the sample rely strongly on the surface properties, the comparison with EDX can reveal the difference of bulk and surface composition, even though the particles are 10 nm in diameter. XPS quantifications showed a systematically higher Ag content in comparison to EDX, which led to the assumption that an Ag enrichment had occurred on the surface of the AgAu nanoparticles, even though the Ag-Au system is perfectly miscible. This hypothesis is supported by quantitative approximations of plasmon peak positions in UV-vis spectra shifting with the composition (see Fig. 7), which can be controlled with the pressure inside the GAS [21].

4 Example Characterization of Double Barrier Memristive Devices

In this section, an extensive investigation of double barrier memristive devices (DBMDs) is presented, from which knowledge-based improvements could be derived. These DBMDs were designed with an active layer (i.e., NbO_x or HfO_x) that is deposited on the bottom part of a Josephson junction ($Nb/Al/Al_2O_3$) [17] and a Schottky-type contact to an Au top electrode. This device is believed to show interfacial resistive switching which is reported to result from oxygen ion movement affecting the interfacial properties [22]. Therefore, no fingerprints for resistive

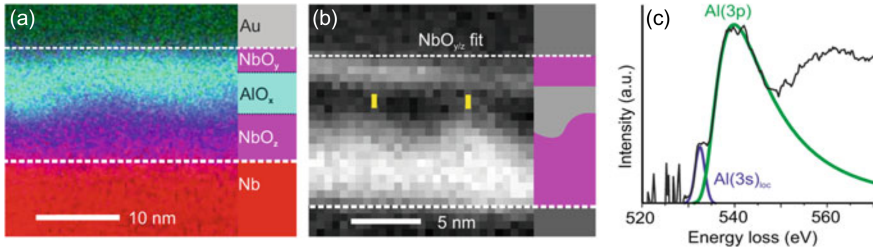

Fig. 8 STEM and spectroscopic investigations of the first generation DBMD. The compound map from EDX signals in **a** illustrates the layout of the device. The goodness-of-fit map in **b** of the O-K edge of the $NbO_{y/z}$ shows the surface-oxidation of the Nb bottom electrode and its roughness. The O-K edge of AlO_x in **c** contains a pre-peak feature which was fitted with a Gaussian function, while the main edge was fitted with a Pearson I(V). Adapted with permission from AIP Publishing [19]

switching, such as filaments that could be directly observed with TEM, are known to characterize these devices.

These devices were analyzed by spatially-resolved STEM-EELS and -EDX to simultaneously map light and heavy elements. ELNES (energy loss near edge structure) fingerprinting was utilized to determine the oxidation states of the Nb atoms. In this approach, the shape of the edges is compared to known reference spectra. In the first-generation DBMD, the ELNES of the alumina resembles that of amorphous Al_2O_3. Unlike the targeted (Nb/Al/Al_2O_3)-Josephson junction, the entire Al layer and even the surface of the Nb bottom electrode are oxidized. This niobia (NbO_z) could be assigned to Nb(II) oxide, thus providing sufficient conductivity for device functionality. The Nb bottom electrode and Al layer were sputtered as metallic thin films, which subsequently oxidize during the reactive sputtering of the memristive layer on top (i.e., NbO_x). However, the ELNES of this NbO_x could not be clearly assigned to a certain Nb oxide. A mixture of Nb(IV) and Nb(V) appears probable. Further, the electronic structure of the AlO_x layer measured with EELS contains an additional pre-peak feature at the O-K edge which is located roughly 6 eV before the main edge (see Fig. 8c). A similar feature, which evolves due to beam damage in oxides, is reported in literature - its origin will be discussed in more detail later on [23, 24]. In this case, however, beam damage appears unlikely, as no evolution of this pre-peak over time and no morphological changes even after extended electron irradiation could be observed. Another explanation of this pre-peak feature could be oxygen vacancies in AlO_x as suggested by Nigo et al. [25]. This feature might be caused by localized Al(3s) states in the band gap of AlO_x. By comparing the area ratio of the pre-peak and of the main edge, the concentration of these vacancies could be estimated to be in the range of 1.7 to 3.2% with respect to the entire oxygen content [19]. A third possible explanation for this feature is a superposition of the O-K edges of alumina and the neighboring niobia, which was observed by Bruley et al. [26]. The onset of the O-K edge from niobia lies few electron volts lower than that of alumina. This explanation seems quite convincing, as the Nb-M_3 and Nb-M_2 edges are present at the same position and the shape and the position of the pre-peak

resembles the onset of the two neighboring niobia O-K edges. Both interdiffusion as well as an imperfectly aligned FIB lamella with respect to the electron beam could explain this scenario.

In addition to spectroscopy, simultaneous morphological analysis can yield further valuable information. The roughness of the bottom electrode leads to a minimal distance between NbO_x and NbO_z of around 1 nm across the AlO_x (see Fig. 8, the yellow lines), which might enable tunneling through this oxide. In contrast to the targeted Nb/Al/Al_2O_3, no metallic Al smooths the interface to the dielectric AlO_x [27] which should lead to an inhomogeneous electric field between the electrodes.

According to [19], these devices demonstrated a high robustness regarding variations from the targeted design and layer sequence. These DBMDs were still functional after NbO_x was subsequently replaced by HfO_x.

Nevertheless, only devices within a central area of a 100 mm wafer were functional (inner red area in Fig. 9a). To understand the reason for this, plasma and TEM characterizations were carried out and revealed distinct differences. In particular, the reactive plasma process to deposit NbO_x layers with metal targets using an Ar / O_2 gas atmosphere leads to variable oxidation states of Nb atoms across a whole wafer [13]. The subsequently patterned devices are showing a distinct memristive functionality in the center of the wafer, while the devices at the edge of the wafer exhibit no memristive I(V) characteristics. These findings indicate a strong correlation between local plasma parameters and device performance and may pave the way to plasma-engineered memristive components in the future. In case of NbO_x, the ELNES of the O-K edge varies between different wafer positions. In the functioning device from the center of the wafer, the ELNES could be assigned to either Nb(IV) or Nb(V) oxide, with slight deviations to both. A mixture of both oxides is probable. However, from a non-functional device from the edge of the wafer (see I(V)-characteristics in Fig. 9d), the O-K edge could not be assigned to a certain oxidation state. The lower signal-to-noise ratio in comparison to the other oxides with the same acquisition parameters, however, suggests a lower Leerschritt O-K edge signal and with this a lower oxidation state of the Nb atoms. In addition, niobium oxide with a low valence state is known to be a conductor and cannot be used to build a Schottky type barrier as observed from the I(V) characteristics [13]. In summary, it could be proven that the EEL spectroscopy of the niobium oxide O-K edge could explain the different at the specific locations on the wafer.

Independent from the top-most oxide (i.e., NbO_x or HfO_x), the AlO_x layer underneath could be assigned to amorphous Al_2O_3 by the O-K edge. However, exactly in the middle of the AlO_x thin film a pre-peak feature appears as shown in Fig. 10a, which clearly differed from the pre-peak from previous studies as shown in Fig. 8c. Pre-peaks of the O-K edge occupied researchers for a long time, but still, the origin and meaning are under debate. The pre-peak can be part of the main O-K edge in some minerals, instead of being an additional defect feature, as shown by Winkler et al. using DFT calculations, e.g., for Hambergite ($Be_2BO_3(OH)$). They have further demonstrated that the "pre"-peak originates not only from the OH-, but also from all BO_3-groups [28]. An older hypothesis from [29], which claimed that the hydrogen content of minerals can be determined from the pre-peak feature, can therefore be

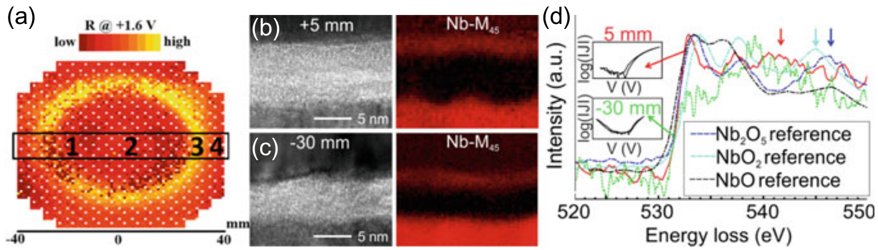

Fig. 9 **a** Resistance map of a whole wafer with memristive devices deposited on top measured at 1.6 V. **b** and **c** HRTEM micrographs from positions comparable with 2 and 3, respectively, indicated in **a**. The STEM-EELS maps of the Nb-M45 edge showing the Nb distribution. **d** illustrates the O-K EEL spectra in the niobiumoxide of the different positions overlaid with reference spectra. The I(V)-characteristics of these devices at the respective positions are shown in the insets. Adapted with permission from American Vacuum Society [13]

ruled out. The same conclusion was stated by Garvie, who assigned the pre-peak of the O-K edge in OH- and H_2O-bearing minerals to beam damage, which could, however, be prevented by low dose-rates [30]. The pre-peak appearing as a result of beam damage originates from the transition of core electrons to unoccupied pi* orbitals of molecular oxygen [23, 31–33], which develops, e.g., due to the decomposition of hydroxides [24] or the reduction of the oxide itself [34, 35]. As indicator for beam damage serves its development over time, as the damage process occurs gradually and the resulting O_2 gas is emitted into the vacuum. A more detailed look on beam-induced damage is provided in the following Chap. 5. A recent study from Ayoola et al. proposed that peroxy O-O bonds developed at the surface of γ-Al_2O_3 in the areas damaged by electron irradiation. However, these O-O bonds could be prevented by employing cryogenic-EELS although beam damage in form of hole drilling still occurred [36]. Peroxy groups were also found in amorphous Al_2O_3 by stochastic quenching simulations which best explains a similar pre-peak of the O-K edge measured by Near Edge X-ray Absorption Fine Structure [37]. Further, single superoxide ions (O_2^-) were detected in sapphire with electron paramagnetic resonance after neutron-irradiation, proving their possible existence in Al_2O_3 [38]. It seems likely though, that peroxy groups in Al_2O_3 are unstable in the electron beam and directly decompose into molecular oxygen. Fritz et al. reported on an electron beam stable pre-peak at the grain boundaries of polycrystalline Al_2O_3, and it was interpreted as chemisorbed molecular oxygen [39].

In our own measurements, the pre-peak in the amorphous Al_2O_3 in the DBMD (Fig. 10a) does not emerge or increase over time, but disappears with electron beam irradiation (see Fig. 10a), which could be an indicator for adsorbed oxygen molecules released to vacuum. This hypothesis is supported by the difference spectrum before and after electron irradiation in Fig. 10a, which resembles the O-K edge of molecular oxygen gas. The pre-peak does not only disappear in the vicinity of the electron beam, but also in distances further than 50 nm, which can be seen in the pre-peak spectral image in Fig. 10e with an exposure time of 100 ms. Here, the oxygen

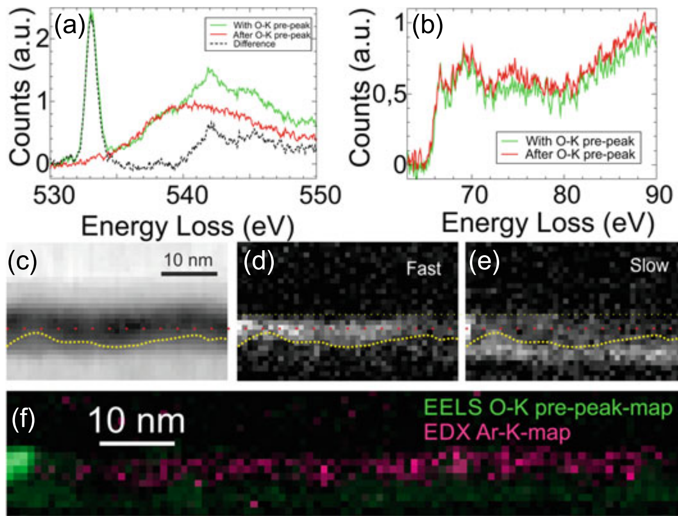

Fig. 10 **a** Time-series of the background-subtracted O-K edge in Al_2O_3 with pre-peak feature (green) in the beginning and after the pre-peak vanished (red). The difference of these spectra (black dashed line), after alignment of the onset of the main O-K edge, resembles the O-K edge of oxygen gas. The Al-L_{23} edges in **b** recorded simultaneously with **a**, show no significant difference, indicating no valance change of Al_2O_3 and no metallic fractions. The STEM-HAADF image in **c** provides an overview for the sequential spectral images of the pre-peak of the O-K edge in **d** and **e**. **d** was recorded first with an exposure time of 9.8 ms and **e** was recorded second with an exposure time of 100 ms. In fast measurements the pre-peak appears spread throughout the entire Al_2O_3, while in slow measurement, the pre-peak concentrates at the left corner where the scan started. The yellow dashed line indicates the interface to the Nb bottom electrode and the orange dashed line indicates the center of the Al_2O_3 where the pre-peak is located. The oxidized Nb bottom electrode shows intensity in the oxygen pre-peak spectral image in **e**, because the onset of the main O-K edge of niobium oxide is located at the same energy. In the compound map **f**, the O-K pre-peak (similar to **e**, but different position) and the Ar EDX signal are anticorrelated. No Ar is detected where the O-K pre-peak concentrates but elsewhere Ar does not vanish

pre-peak concentrates at the left corner, from where the scan was initiated, while a fast measurement beforehand (Fig. 10d) proved that the pre-peak spreads over the entire Al_2O_3. This long-range effect could be explained by two scenarios. In the first, secondary electrons spreading in all directions from the focused electron beam, which causes the pre-peak to vanish before it could be measured in EELS. These secondary electrons have lower energy and a shorter mean free path and may produce stronger beam damage by radiolysis (for more details see Sect. 5 about beam damage). In the second scenario, the focused electron beam positively charges [35] the Al_2O_3, which could attract negatively charged chemisorbed [40, 41] oxygen-gas molecules.

An argument for the second scenario is that the intensity of the concentrated pre-peak appears higher, when comparing the second, slower scan to the initial fast scan. This could be explained by the attraction of negatively charged chemisorbed

oxygen, not only from the right side of the scanning window in the Al_2O_3 but also from the left. In a time-series (see Fig. 10a), no further increase in the pre-peak was observed but only a decrease, which argues against a development over time and therefore against a pre-peak produced by beam-damage. In the pre-peak-map in Fig. 10e, intensity can be observed below the yellow dashed line, roughly indicating the interface to the Nb bottom electrode. However, this intensity is produced from the main O-K edge of the oxidized Nb, which is located at the same energy and therefore mapped as well. In the fast measurement in Fig. 10d the noise level is too high to detect the Nb O-K edge.

The presence of Ar gas inside the Al_2O_3 further proves the possibility for gas inclusions and thus for incorporated oxygen gas. Ar gas was detected at the same position as the molecular oxygen in the middle of Al_2O_3 by EDX and EELS (compare Fig. 6). The Ar signal disappears, however, where the O-K pre-peak concentrates, even though Ar gas is present where the O-K pre-peak has vanished by the long-range effect (see Fig. 10f). This may indicate a physical displacement of the Ar atoms from the oxygen molecules, as the Ar signal is stable in the electron beam. However, molecular oxygen could have also been formed due to the preparation, where the Ar atoms could destabilize the Al_2O_3 as proposed by Nufer [15]. In this case, the molecular oxygen should be the product of the reduction of Al_2O_3 to metallic Al, but no temporal changes at the Al-L_{23} edges, indicative for metallic Al [34], could be observed in the EELS time series of the Al-L_{23} edges in Fig. 10b. Since the TEM sample preparation was done without Ar ions, the origin of the incorporated Ar can be attributed to the sputter gas of the deposition process. We assume, Ar atoms implanted during reactive HfO_2 sputtering, where the Al and the top-most Nb back electrode were oxidized, as no traces of Ar could be found in the metallic Al thin film.

The extensive analysis of a memristive device examined various aspects. These include the oxidation and roughness of the Nb bottom electrode as well as different oxidation states of the NbO_y in dependence on the position of the device on the wafer which lead to malfunctions. However, the switching mechanism could not be resolved with TEM due to its interfacial character with very small dimensions and amorphous structure. Last but not least, gas inclusions inside the 7 nm Al_2O_3 consisting of Ar and most probably molecular O_2 were indicated by EDX and EELS, whether these are important for the resistive switching will be investigated in future.

5 Invasive TEM Measurements

The TEM utilizes the interaction of accelerated electrons with solid matter to facilitate imaging with sub-Å spatial resolution. Due to the highly energetic impact, sensitive materials can be severely damaged by prolonged irradiation. Especially at high dose-rates, the induced beam damage can limit the resolution and available time for TEM analysis. The following chapter introduces a broad overview of different mechanisms

of beam damage, which is followed by practical examples from memristive devices, and reasons, why they require special care.

5.1 Beam Damage Overview

Electron beam damage typically describes irreversible changes in the investigated sample during TEM analysis. A variety of phenomena can occur, like surface sputtering, phase transformations, (re)crystallization or amorphization, valence changes and gas bubble formation. In general, beam damage can occur via two different mechanisms, which may develop simultaneously and often cannot be clearly distinguished. The first mechanism is the so-called knock-on damage, where collisions of electrons cause an elastic displacement of atoms. The second mechanism occurs due to the inelastic interaction of beam electrons with core electrons, leading to the formation of an excited state. This effect is called radiolysis. Electron beam damage in the TEM was reviewed by Egerton [42] and Jiang [43]. This chapter discusses important aspects of beam damage in relation to the materials used in memristive devices and how it may be prevented.

Knock-on damage occurs preferentially at the surface due to the lower binding energy of surface atoms, and preferential sputtering is expected in compounds of the elements with the lower binding energy [42]. As a 'rule of thumb', knock-on damage increases with increasing beam energy while the effects of radiolysis decrease. Radiolytic damage occurs predominantly in dielectrics with low conductivity, as the excited state has a longer lifetime to produce point defects compared to conductive materials. In the vicinity of the beam the excited states accumulate and create a charged area - typically positively charged in TEM due to secondary and Auger electron emission. This positive charge can lead to cation migration away from the irradiated area and, e.g., the creation of molecular oxygen [23, 34].

Different parameters influence the beam damage. As mentioned before, the acceleration voltage determines which of the two damage mechanisms dominates. With increasing acceleration voltage an increased maximum energy can be transferred during interaction with an atomic nucleus leading to displacement and thus knock-on damage. On the other hand, inelastic scattering is reduced which reduces charging in dielectrics and the number of atoms in an excited state. Dielectrics typically charge up positively in the TEM [44], as most fast electrons are transmitted through the sample and secondary (SE) and Auger electrons are created. In thicker samples or especially in the SEM this positive charge can be compensated by absorbed electrons from the primary beam leading to negative charging [45]. The cross-section for SE emission has a maximum at several keV and decreases with the acceleration voltage, as the mean free path of the electrons increases [46]. Accordingly, charging and thereby radiolysis can be reduced with higher acceleration voltages and particularly thin specimens provide a further means of mitigation. Beam damage is further affected by the dose (accumulated electrons per unit area) as well as the dose-rate (accumulated electrons per unit area and unit time or also called current density of

the electron beam). The excited state requires sufficient energy for atomic displacements, while the life-time and localization need to be high enough so that an atom can move after the energy is converted into momentum [44]. Accordingly, radiolysis mainly affects insulators, as lifetime (and localization) are too short in conductors, where the excited state is rapidly relaxing. However, in insulators excited atoms may change their valence state or start to move. For reversible processes (in the sense of damage and recovery), the dose-rate determines the damage. Significant damage only occurs if the activation is faster than the recovery. In this case, it is sufficient to reduce the dose-rate to prevent beam damage, although the accumulated dose after prolonged measurements can be high [32]. However, it is not necessarily the case that the recovered and the original state are identical. The simplest way to reduce the dose-rate is to analyze the sample at low magnification. In case, high resolution is relevant, the beam current (spot size) needs to be reduced until no damage occurs. The following chapter describes examples of beam damage occurring in different material classes used for memristive devices.

5.2 *Thin Film Metal Layers in TEM*

Metals mainly suffer from knock-on damage, which can be easily reduced by employing low acceleration voltages. However, most metals are commonly covered with a thin oxide layer, and in the case of silver even with a sulfide layer. These compounds can be decomposed by the electron beam, leaving mobile silver nanoparticles on the surface. TEM experiments were performed at the tip of an intact atomic force microscope (AFM) apex. The apex is coated with a gold thin film as electrode, a silver thin film as active metal and a SiN_x-matrix as insulating layer. This so-called Memtip-approach enables the investigation of the very same conducting filament with different counter-electrodes [47]. The TEM experiments revealed the invasive character of the electron beam making ex situ measurements before and after conductive AFM (c-AFM) not feasible. After 15 min of electron beam irradiation with 200 kV acceleration voltage silver protrusions and morphological as well as chemical changes in the SiN_x-matrix had developed (see Fig. 11a, b). The matrix became denser and thinner, and in EDX, no nitrogen could be detected. Instead, oxygen was found, which suggests that the pristine matrix was porous and did not entirely protect the silver from the atmosphere. It is likely that atmospheric sulfur formed some Ag_2S under the matrix, which is known to build Ag protrusions under electron beam irradiation due to mobile Ag^+ ions inside Ag_2S and injected electrons [48–50]. Accordingly, samples containing silver should be transferred and stored with particular care prior to analysis, e.g., by using a vacuum transfer holder. A different approach is to seal the surface in situ with a non-porous matrix to prevent oxidation and surface migration, as reported in [51]. Otherwise, such morphological changes can lead to the misinterpretation of ex situ or in situ biasing TEM experiments since these morphological changes can already be formed by contact with the atmosphere

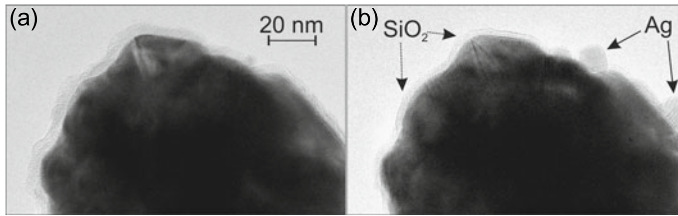

Fig. 11 AFM apex before **a** and after **b** TEM and EDX measurements. In **b**, arrows on the right indicate evolving Ag protrusions and arrows on the left indicate morphological and chemical changes of the SiN_x matrix [47]

or by the electron beam. Accordingly, ex situ or in situ TEM experiments should be reproduced without electrical stimuli.

5.3 Oxides in the TEM and SEM

The key component in a multitude of vertical memristors is a dielectric thin film [52]. Because of this, special care should be taken when analyzing these dielectrics in the TEM, and, of course, also during imaging and preparation in the SEM. The following section describes various phenomena that can occur with oxides in the electron beam, especially when they are produced with high defect concentrations.

5.3.1 Crystallization of Amorphous Oxides

The active oxide in memristors being amorphous can be beneficial, as the amorphous state is isotropic in comparison to the granular microstructure of polycrystalline thin films. Further, the processing costs can be reduced due to the lower deposition temperatures of amorphous films. As a model system to be analyzed, amorphous hafnia was chosen, which represents one of the most studied high-k oxides in many fields, including resistive devices [53, 54] as well as ferroelectric applications [55].

Mittmann et al. observed that radio frequency (RF) sputtering of hafnia leads to sub-stoichiometric, amorphous hafnia thin films, which can crystallize in the ferroelectric orthorhombic ($Pca2_1$) phase after rapid thermal annealing (RTA). However, when sufficient oxygen is added during the deposition, the monoclinic equilibrium phase is obtained [55]. We observed the crystallization of the pristine amorphous hafnia thin films during the TEM measurements, which appeared more pronounced at higher magnification (i.e., with higher dose and dose rate). Figure 12a shows such a crystallized region after 15 min of imaging in high-resolution mode. The crystallization starts from the very beginning of electron beam irradiation, though. The selected area diffraction (SAED) inset indicates a polycrystalline phase-mixture of hafnia. This thin film was RF sputtered with Ar from a hafnia target after a condi-

tioning time of 10 min to reach a steady state on the target surface. However, when the target was pre-treated with a mixed oxygen-argon-plasma to increase the oxygen content, the thin film exhibited few nanocrystallites in the pristine state which could serve as nucleation center for crystallization. Nevertheless, no crystallization caused by the electron beam was observed (see Fig. 12b). We hypothesize that the chemical composition has a significant effect on the beam-induced crystallization of the investigated hafnia. The same is true for the crystalline phase after RTA. Admixture of sufficient oxygen leads to the monoclinic phase while a sub-stoichiometric hafnia can crystallize in the orthorhombic phase [55].

Investigations with different substrates were performed to evaluate their influence on the crystallization, e.g., the influence of charging and oxygen-absorption. These substrates include amorphous carbon, amorphous Si_3N_4 and polycrystalline TiN, which is also serving as back-electrode in metal-insulator-metal (MIM) structures. On the amorphous carbon layer of a standard TEM grid a lot of nanocrystallites were present as-deposited, while the electron beam still induced strong crystallization of the thin film (see Fig. 12c). The same is true for hafnia on polycrystalline TiN thin film (see Fig. 12d). These findings underline that the nanocrystallites are no prerequisite for electron beam crystallization. Of higher importance is the stoichiometry of the thin film.

Further, a simple heating effect as cause for the crystallization in the electron beam can be ruled out. After prolonged heating instead of electron irradiation a pure,

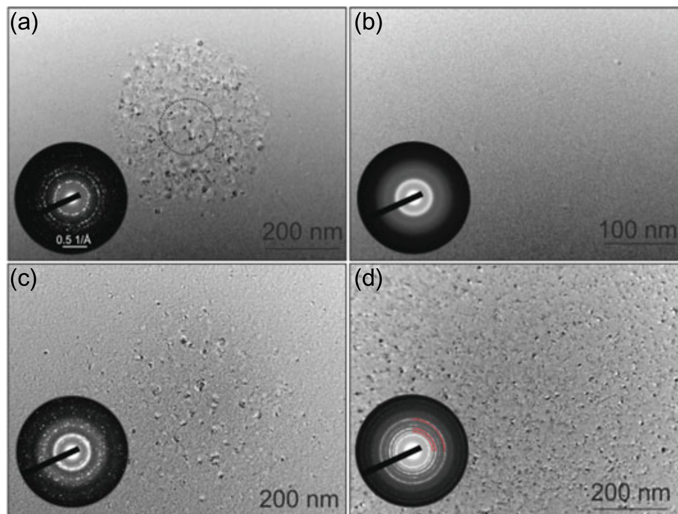

Fig. 12 TEM images of an amorphous, RF-sputtered HfO_x thin film on various substrates after up to 15 min of electron beam irradiation. In **a** and **b**, the thin film was sputtered on a Si_3N_4 membrane, in **c** on amorphous carbon and in **d** on a Si_3N_4/TiN thin film stack. In **b**, the thin film is showing no crystallization in the electron beam, but a few nanocrystals are present in the pristine state. In this case, the ceramic target was pre-sputtered with oxygen admixture. The insets show SAED patterns with diffraction rings of TiN in **d** beeing indicated with red arcs

thermodynamically stable monoclinic HfO_2 is expected [56]. In our examination, the thin films with higher oxygen content should crystallize as well due to a heating effect, which is not the case. In addition, several studies indicate that the temperature increases by no more than 10 °C during normal imaging conditions [42, 44, 57–59].

As a cause for the crystallization, radiolysis seems to be likely, as different studies reported on the occurrence of crystallization when amorphous oxides were reduced in the electron beam [60, 61].

However, this beam crystallization is not affected by whether the substrate is conductive (TiN and amorphous carbon) or insulating (Si_3N_4). Accordingly, a subsequent charging effect does not play a major role for the crystallization.

Taking these investigations into account, we propose that only the initial oxygen content, or, in terms of oxygen vacancies, the defect concentration, determines the crystallization of the amorphous HfO_x in the electron beam and also the resulting phase after annealing. However, an unambiguous statement is hardly possible. Further triggers for crystallization could be, e.g., the amorphous structure, free volume and presence of nucleation centers.

A second example for defect concentration-dependent beam damage was already discussed in Sect. 2. Here, Ar-milling with energies above 3 keV can alter crystalline Al_2O_3 in a way that it becomes susceptible to beam damage [14]. These findings highlight that the defect-concentration has a major impact on the stability of the sample in the TEM. This could be explained by the increasing free volume due to the defects leading to higher diffusion rates due to lower activation energies. On the other hand, beam damage produces defects. One example is a ferroelectric $BaTiO_3$ thin film that can be converted into a memristive thin film with configurable resistive states by electron beam irradiation [62].

5.3.2 Hole-Drilling and Oxide Reduction

In STEM mode, the focused electron beam has a high dose-rate (current-density), which can be more destructive in comparison to the TEM mode. In Fig. 13a, the electron beam produced a line of holes after an EDX line scan across a HfO_2 thin film with a dwell time of 6 s at each position. Close to the dark area of the holes in the STEM image, high intensity in the vicinity gives an indication for the formation mechanism of these holes. Cazaux proposed a possible mechanism, starting with the accumulation of positive charges, which occur due to secondary and Auger electron emission in the vicinity of the electron beam [35]. These positive charges repel cations, creating an excess of anions which can react to molecular oxygen [23, 34]. Following this mechanism, the bright Z-contrast next to the holes in Fig. 13a may hint towards a thicker crater rim with Hf-excess.

Such a reduction mechanism is dose-rate-dependent so that below a certain, material-dependent threshold, no visible beam damage occurs [32] and recovery processes can compensate the damage [33].

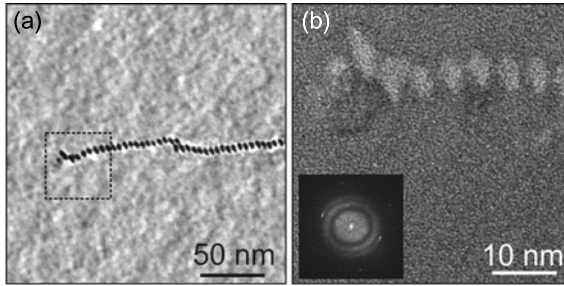

Fig. 13 **a** STEM image showing hole drilling in an amorphous HfO_2 thin film after a line scan. **b** HRTEM micrograph and FFT-inset reveal crystalline regions around the holes

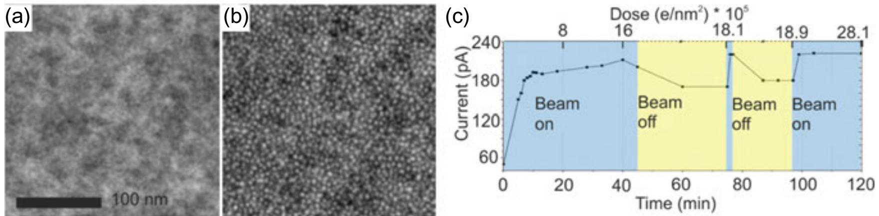

Fig. 14 **a** and **b** EFTEM (at 17 eV energy loss) images of a PECVD-deposited SiO_2 thin film after doses of 1.3 and 22 Me/nm^2, respectively. In **b**, silicon-rich nanoparticles develop at the bright dots. **c** Electron beam-induced conductivity changes of the same SiO_2 film. Current was measured at 3 V. Adapted with permission from Cambridge University Press [63]

The following section describes a tool which can be used to measure this threshold in situ in the TEM or SEM. This threshold becomes particularly important when defect concentrations or defect variations are to be measured (e.g., using EELS). The (partial) reduction of oxides is equivalent to the generation of oxygen vacancies, which are commonly discussed point defects involved in the memristive switching mechanism. In addition, the thresholds for stoichiometric oxides reported in literature [42] will vary significantly from defective oxides. For this purpose, in situ electrical measurements on several thin film oxides were carried out, revealing reversible changes in conductivity attributed to a reduction in the electron beam and subsequent re-oxidation of the materials (see Fig. 14c). In case of SiO_2 thin films, the electron dose-induced formation of Si-rich particles leads to an increase in conductivity [63]. This effect can be reversed upon exposure to the atmosphere and even in the vacuum of the TEM when the beam is blanked. In the blue regions of Fig. 14c, the conductivity is increased during electron beam irradiation, while in the yellow areas, the conductivity is decreased upon blanking the beam. The chemical changes are indicated by energy-filtered (EF)TEM dose series showing Si nanoparticle formation by filtering the Si plasmon peak at 17 eV. Applying a dose of 22 Me/nm^2 white dots have evolved gradually in Fig. 14b indicating the formation of particles. The conductivity change caused by irradiation can be utilized to determine the critical dose for beam

damage, thus providing data for the inhibition of such effects. This can be used prior to in situ or *in operando* TEM and SEM experiments with ceramics to prevent beam effects on the I(V) characteristics and morphology. Due to this reversible behavior of the electron beam on the I(V) characteristics we labeled this experiment as the TEMristor. In these measurements, the beam damage was dominated by radiolysis, as indicated by the dependence on the acceleration voltage. The critical dose decreases with the acceleration voltage. Especially in the SEM with voltages of 30 kV and lower, e.g., TiO_2 exhibits a lower critical dose compared to 300 kV in the TEM.

This observation reconnects to the TEM preparation in Sect. 2 and highlights that dielectrics may have already been damaged by the electron beam during FIB-preparation. An effect that should be reduced by applying low beam-dose as well as a conductive coating on the sample.

5.4 Conclusions of Electron Beam Effects

In this chapter different mechanisms for beam damage in the TEM were described. Metallic samples are more prone to knock-on damage while dielectrics are more prone to radiolysis. In the context of memristive devices with high defect concentrations, either specially-designed or produced on purpose through a formation step, beam damage is a major concern: The included defects facilitate the beam damage, especially in the regions of interest where the memristive switching occurs. Low-dose rates should therefore be chosen to investigate memristive devices, either to prevent or at least reduce the beam damage. In situ current measurements can be used to determine the threshold below which no significant damage occurs. Further aids and best practices will be described in the next chapter.

6 Solutions

Materials can be sensitive to damage induced by either TEM sample preparation via FIB and Ar ion milling, or even the TEM measurement itself – this holds especially true for thin films designed for memristive devices, i.e., in non-equilibrium states and with high defect concentrations. In this section, different approaches for reliable TEM analysis of memristive devices are proposed.

6.1 Ex situ Measurements on Horizontal Devices

The best way to verify the reliability of TEM measurements of memristive devices, and to exclude severe alterations by the preparation or the electron beam is to electrically characterize the TEM specimen before and after in an ex situ manner. This

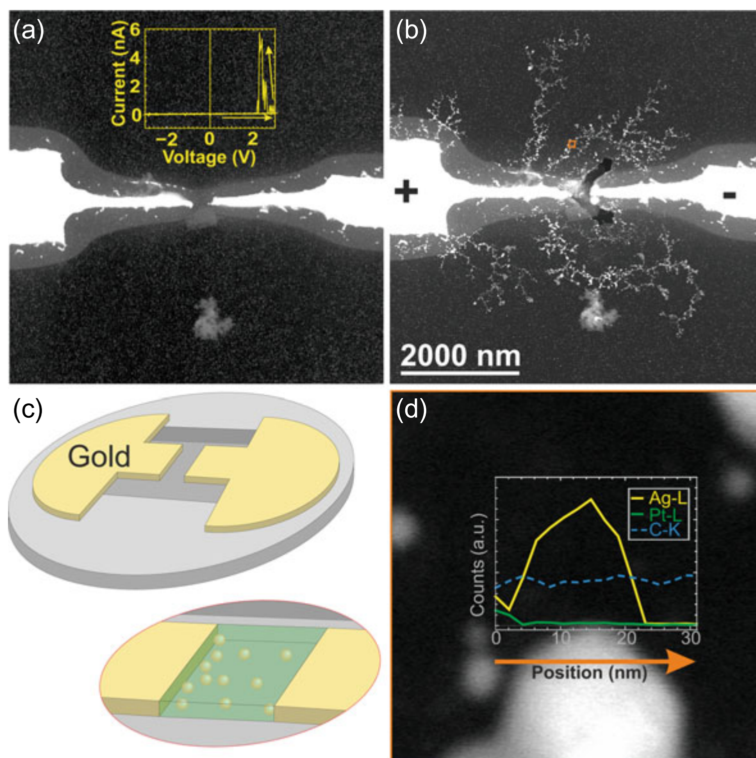

Fig. 15 Overview STEM image before **a** and after **b** ex situ electrical probing. Bimetallic AgPt nanoparticles were deposited by a Haberland cluster source on top of the electrodes and these were covered with a SiON-matrix. The inset in **a** shows the I(V)-characteristics of the dielectric break down. The schematic design of the ex situ grids with structured Au contracts on Si_3N_4 membranes is illustrated in **c**. An EDX linescan in **d** along the orange arrow reveals that the fractal dendrites consist mainly of Ag. The position of **d** is indicated by the orange square in **b**. Adapted by permission from [Springer Nature Customer Service Centre GmbH]: [Springer] [64]

approach can be realized via a horizontal electrode design which can be lithographically structured on electron-transparent Si_3N_4 membranes. Such an electrode design is illustrated in Fig. 15c. The detailed procedure is described in reference [64]. By means of electron beam lithography electrode distances of 40 nm and below were achieved, which enable a good observation of the region of interest at high resolution. The corresponding prototype, deposited via, e.g., sputtering, can subsequently be analyzed in the TEM. Following this approach, it was possible to observe fractal growth in an AgPt nanoparticle film below the percolation limit, encapsulated in a SiON-matrix which suffered a dielectric breakdown during electrical probing. EDX measurements in Fig. 15c revealed that these fractal dendrites consist of silver and leave behind Pt-rich nanoparticles after electrical biasing. This observation provides information for the switching mechanism of a similar, but vertical nanoparticle-based

diffusive memristor [65]. In bimetallic nanoparticles, the less noble metal mainly contributes to the filament formation while the noble counter part remains behind and can serve as an anchor point for the filament to enhance memristive switching [21]. However, this ex situ approach may be insufficient, as a (partially) reduced oxide might re-oxidize during transfer to the ex situ measurement setup and electron beam damage could go unnoticed. To be sure, in situ or *in operando* experiments are necessary, and suitable approaches are described in the following section.

6.2 FIB Preparation for In situ Experiments

A horizontally-arranged prototype device may serve well for TEM measurements and fundamental research, but is not comparable to real devices, as the geometry of the electrodes has a major impact on the properties of the device [66]. For this purpose, the real devices have to be analyzed and to exclude preparation artefacts, the functionality of the TEM sample should be checked and compared to the device. TEM sample preparation for *in operando* experiments on vertical devices requiring FIB turned out to be a major obstacle due to Pt and Ga contamination and material re-deposition, all creating possible short circuits. To overcome these problems, the sample geometry and a specially adapted MEMS chip for in situ electrical biasing were designed by Zintler et al. [67]. The preparation improvements start with a special stub, mounting both the sample and the MEMS chip orthogonal to each other. This stub enables venting-free preparation including lift-out, transfer, contacting of the electrodes and thinning. Top and bottom electrodes are contacted with Pt trenches from the gas injection system in the FIB instrument. To prevent short circuits and memristive switching apart from the electron transparent region, the counter electrodes are cut next to the Pt trenches by means of Ga-ion etching. The whole preparation is described in detail in [67]. After successful preparation, the lamella can be electrically characterized in situ or even *in operando* in the TEM and the comparison of the lamella device with the macro device shows striking similarities (compare Fig. 16b, c with f, e). Further, the influence of the electron beam can be measured electrically.

Despite these striking similarities, the approach also presents some drawbacks. First, the preparation is time-consuming and is likely to end up in a short circuit. Secondly, the lamella device is quite large, and the resistive switching therefore difficult to observe, as it may occur at any point in the lamella. This second point is not only a drawback, as the geometry is not altered significantly and a larger area can be observed. Further, such a lamella has two free surfaces which may dominate the switching when diffusion or migration is involved. And last but not least, the small dimensions make Joule heating more critical which may lead to a faster device degradation and could limit TEM observations [67].

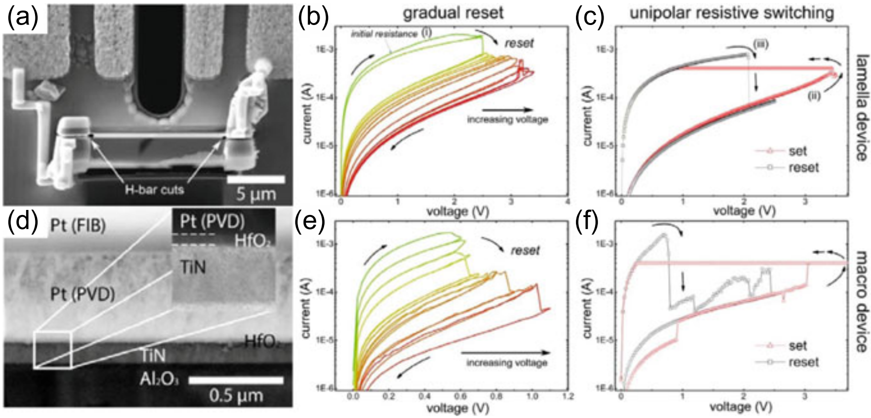

Fig. 16 **a** FIB lamella mounted and contacted by Pt trenches to contacts of the MEMS chip. **d** STEM image of the device for the in situ measurements. The inset shows a Bright-field STEM image with higher magnification. **b** and **c** show I(V)-characteristics of the lamella device while **f** and **e** represent data for the macroscopic device. **b** and **f** show the gradual reset and **c** and **e** the unipolar resistive switching. Adapted with permission from Elsevier [67]

6.3 Conclusions and Best Practice

In conclusion, reliable TEM experiments on memristive devices can be realized by adhering to the following guidelines:

- Surface diffusion processes must be prevented, e.g., by the application of barrier layers on the top and bottom of the devices, cf. [51].
- Contamination of the samples must be prevented, e.g., by using suitable device transfer systems from the sputtering devices to the TEM.
- If possible, check for functionality before and after preparation and after the TEM-measurements. For this purpose, horizontal instead of vertical devices should be produced and analyzed. These systems do not require sophisticated TEM preparation, since they can be fabricated directly for TEM analysis.
- For real device characterization, electrically contacted FIB lamellas should be analyzed *in operando* and the I(V)-characteristics should be critically compared to the real device.
- In ex situ, in situ or *in operando*, experiments, current measurements should be used to determine the threshold for electron beam damage. If this is not possible, the usage of low dose rates but high acceleration voltages is advisable, if dielectric memristive devices are to be characterized.

7 Experimental

TEM measurements were performed on different microscopes. High-end EELS for the DBMD characterization was done on a FEI Titan[3] provided by ESTEEM3 facilities. Acceleration voltages of 300 kV and 80 kV were used in conjunction with a monochromator, XFEG, GIF quantum energy analyzer and SuperX EDX detector. The analysis of the electron beam crystallization of hafnia thin films was conducted on a JEOL JEM-2100 with 200 kV and a LaB_6 cathode. Hole-drilling experiments, also with hafnia thin films were performed using a Tecnai F30 G^2 microscope with 300 kV and a field emission gun.

Acknowledgements This project has received funding from the European Union's Horizon 2020 research and innovation programme under grant agreement No 823717 – ESTEEM3. The financial support by the German Research Foundation (Deutsche Forschungsgemeinschaft—DFG) through FOR 2093 is gratefully acknowledged. Funded by the Deutsche Forschungsgemeinschaft (DFG, German Research Foundation) – ProjectID 434434223 – SFB 1461.

References

1. Kendall, J.D., Kumar, S.: The building blocks of a brain-inspired computer. Appl. Phys. Rev. **7**, 011305 (2020). https://doi.org/10.1063/1.5129306
2. Sebastian, A., Le Gallo, M., Khaddam-Aljameh, R., Eleftheriou, E.: Memory devices and applications for in-memory computing. Nat. Nanotechnol. **15**, 529–544 (2020). https://doi.org/10.1038/s41565-020-0655-z
3. Strobel, J., Neelisetty, K.K., Chakravadhanula, V.S.K., Kienle, L.: Transmission electron microscopy on memristive devices: an overview. Appl. Microsc. **46**, 206–216 (2016). https://doi.org/10.9729/AM.2016.46.4.206
4. Yang, Y., et al.: Probing electrochemistry at the nanoscale: in situ TEM and STM characterizations of conducting filaments in memristive devices. J. Electroceramics **39**, 73–93 (2017). https://doi.org/10.1007/s10832-017-0069-y
5. Sun, W., et al.: Understanding memristive switching via in situ characterization and device modeling. Nat. Commun. **10** (2019). https://doi.org/10.1038/s41467-019-11411-6
6. Xu, H., et al.: Dynamic structure-properties characterization and manipulation in advanced nanodevices. Mater. Today Nano **7**, 100042 (2019). https://doi.org/10.1016/j.mtnano.2019.100042
7. Yang, X., et al.: A review of in situ transmission electron microscopy study on the switching mechanism and packaging reliability in non-volatile memory. J. Semicond. **42**, 013102 (2021). https://doi.org/10.1088/1674-4926/42/1/013102
8. Ielmini, D., Waser, R. (eds.): Resistive Switching: From Fundamentals of Nanoionic Redox Processes to Memristive Device Applications. Wiley (2015). https://doi.org/10.1002/9783527680870
9. Du, H., et al.: Nanosized conducting filaments formed by atomic-scale defects in redox-based resistive switching memories. Chem. Mater. **29**, 3164–3173 (2017). https://doi.org/10.1021/acs.chemmater.7b00220
10. Kwon, D.-H., et al.: Atomic structure of conducting nanofilaments in TiO2 resistive switching memory. Nat. Nanotechnol. **5**, 148–153 (2010). https://doi.org/10.1038/nnano.2009.456
11. Li, C., et al.: Dynamic observation of oxygen vacancies in hafnia layer by in situ transmission electron microscopy. Nano Res. **8**, 3571–3579 (2015). https://doi.org/10.1007/s12274-015-0857-0

12. Jang, J.H., et al.: Investigation of oxygen-related defects and the electrical properties of atomic layer deposited HfO_2 films using electron energy-loss spectroscopy. J. Appl. Phys. **109**, 023718 (2011). https://doi.org/10.1063/1.3544039
13. Zahari, F., et al.: Correlation between sputter deposition parameters and I-V characteristics in double-barrier memristive devices. J. Vac. Sci. Technol. B **37**, 061203 (2019). https://doi.org/10.1116/1.5119984
14. Nufer, S., et al.: Quantitative atomic-scale analysis of interface structures: transmission electron microscopy and local density functional theory. Phys. Rev. Lett. **86**, 5066–5069 (2001). https://doi.org/10.1103/PhysRevLett.86.5066
15. Nufer, S.: Spatially Resolved Analytical Electron Microscopy at Grain Boundaries of a-Al2O3 (2001)
16. Kang, H.-J., Kim, J., Oh, J., Back, T., Kim, H.: Ultra-thin TEM sample preparation with advanced backside FIB milling method. Microsc. Microanal. **16**, 170–171 (2010). https://doi.org/10.1017/S1431927610054474
17. Gurvitch, M., Washington, M.A., Huggins, H.A.: High quality refractory Josephson tunnel junctions utilizing thin aluminum layers. Appl. Phys. Lett. **42**, 472–474 (1983). https://doi.org/10.1063/1.93974
18. Ishitani, T., Yaguchi, T.: Cross-sectional sample preparation by focused ion beam: a review of ion-sample interaction. Microsc. Res. Tech. **35**(4), 320–333 (1996). https://doi.org/10.1002/(SICI)1097-0029(19961101)35:4<320::AID-JEMT3>3.0.CO;2-Q
19. Strobel, J., et al.: In depth nano spectroscopic analysis on homogeneously switching double barrier memristive devices. J. Appl. Phys. **121**, 245307 (2017). https://doi.org/10.1063/1.4990145
20. Kiss, K.: Problem Solving with Microbeam Analysis. OCLC: 1058661531. Elsevier Science, Amsterdam (2014)
21. Vahl, A., et al.: Single target sputter deposition of alloy nanoparticles with adjustable composition via a gas aggregation cluster source. Nanotechnology **28**, 175703 (2017). https://doi.org/10.1088/1361-6528/aa66ef
22. Hansen, M. et al.: A double barrier memristive device. Sci. Rep. **5** (2015). https://doi.org/10.1038/srep13753
23. Jiang, N., Spence, J.C.: Interpretation of Oxygen K pre-edge peak in complex oxides. Ultramicroscopy **106**, 215–219 (2006). https://doi.org/10.1016/j.ultramic.2005.07.004
24. Klimenkov, M., Möslang, A., Lindau, R.: EELS analysis of complex precipitates in PM 2000 steel. Eur. Phys. J. Appl. Phys. **42**, 293–303 (2008). https://doi.org/10.1051/epjap:2008084
25. Nigo, S., et al.: Conduction band caused by oxygen vacancies in aluminum oxide for resistance random access memory. J. Appl. Phys. **112**, 033711 (2012). https://doi.org/10.1063/1.4745048
26. Bruley, J., et al.: Investigations of the chemistry and bonding at niobiumsapphire interfaces. J. Mater. Res. **9**, 2574–2583 (1994). https://doi.org/10.1557/JMR.1994.2574
27. Imamura, T., Hasuo, S.: Cross-sectional transmission electron microscopy observation of $Nb/AlO_x-Al/Nb$ Josephson junctions. Appl. Phys. Lett. **58**, 645–647 (1991). https://doi.org/10.1063/1.104556
28. Winkler, B., et al.: Oxygen K-edge electron energy loss spectra of hydrous and anhydrous compounds. J. Phys. Condens. Matter **25**, 485401 (2013). https://doi.org/10.1088/0953-8984/25/48/485401
29. Wirth, R., Wunder, B.: Characterization of OH-containing phases by TEM using electron energy-loss spectroscopy (EELS): Clinohumite-OH, chondrodite-OH, phase A, and the (F, OH)-solid solution series of topaz. J. Trace Microprobe Tech. **18**(1), 35–50 (2000)
30. Garvie, L.A.: Can electron energy-loss spectroscopy (EELS) be used to quantify hydrogen in minerals from the O K edge? Am. Mineral. **95**, 92–97 (2010). https://doi.org/10.2138/am.2010.3290
31. Kosugi, N., Shigemasa, E., Yagishita, A.: High-resolution and symmetry-resolved oxygen K-edge spectra of 0 2. Chem. Phys. Lett. **190**, 8 (1992)
32. Jiang, N., Spence, J.C.H.: On the dose-rate threshold of beam damage in TEM. Ultramicroscopy **113**, 77–82 (2012). https://doi.org/10.1016/j.ultramic.2011.11.016

33. Mkhoyan, K.A., Silcox, J., Ellison, A., Ast, D., Dieckmann, R.: Full recovery of electron damage in glass at ambient temperatures. Phys. Rev. Lett. **96** (2006). https://doi.org/10.1103/PhysRevLett.96.205506
34. Berger, S.D., Salisbury, I.G., Milne, R.H., Imeson, D., Humphreys, C.J.: Electron energy-loss spectroscopy studies of nanometre-scale structures in alumina produced by intense electron-beam irradiation. Philos. Mag. B **55**, 341–358 (1987). https://doi.org/10.1080/13642818708208619
35. Cazaux, J.: Correlations between ionization radiation damage and charging effects in transmission electron microscopy. Ultramicroscopy **60**, 411–425 (1995). https://doi.org/10.1016/0304-3991(95)00077-1
36. Ayoola, H.O., et al.: Origin and suppression of beam damage-induced oxygen-K edge artifact from gamma-Al2O3 using Cryo-EELS. Ultramicroscopy **219**, 113127 (2020). https://doi.org/10.1016/j.ultramic.2020.113127
37. Arhammar, C., et al.: Unveiling the complex electronic structure of amorphous metal oxides. Proc. Natl. Acad. Sci. **108**, 6355–6360 (2011). https://doi.org/10.1073/pnas.1019698108
38. Seeman, V., et al.: Atomic, electronic and magnetic structure of an oxygen interstitial in neutron-irradiated Al2O3 single crystals. Sci. Rep. **10**, 15852 (2020). https://doi.org/10.1038/s41598-020-72958-9
39. Fritz, S., et al.: Correlating the nanostructure of Al-oxide with deposition conditions and dielectric contributions of two-level systems in perspective of superconducting quantum circuits. Sci. Rep. **8**, 7956 (2018). https://doi.org/10.1038/s41598-018-26066-4
40. Malek, A., Eikerling, M.H.: Chemisorbed Oxygen at Pt(111): a DFT study of structural and electronic surface properties. Electrocatalysis **9**, xs370–379 (2018). https://doi.org/10.1007/s12678-017-0436-0
41. Tan, E., Mather, P.G., Perrella, A.C., Read, J.C., Buhrman, R.A.: Oxygen stoichiometry and instability in aluminum oxide tunnel barrier layers. Phys. Rev. B **71** (2005). https://doi.org/10.1103/PhysRevB.71.161401
42. Egerton, R.: Radiation damage to organic and inorganic specimens in the TEM. Micron **119**, 72–87 (2019). https://doi.org/10.1016/j.micron.2019.01.005
43. Jiang, N.: Electron beam damage in oxides: a review. Rep. Prog. Phys. **79**, 016501 (2016). https://doi.org/10.1088/0034-4885/79/1/016501
44. Hobbs, L.W.: Murphy's law and the uncertainty of electron probes. Micro-anal. Microlithogr. **4**, 14 (1990)
45. Zhang, H.-B., Feng, R.-J., Ura, K.: Utilizing the charging effect in scanning electron microscopy. Sci. Prog. **87**, 249–268 (2004). https://doi.org/10.3184/003685004783238490
46. Williams, D.B., Carter, C.B.: Transmission Electron Microscopy: A Textbook for Materials Science, 2nd edn., 4 pp. Springer, New York (2008)
47. Carstens, N., et al.: Enhancing reliability of studies on single filament Memristive switching via an unconventional cAFM approach. Nanomaterials **11**, 265 (2021). https://doi.org/10.3390/nano11020265
48. Liang, C. et al.: Ionic-electronic conductor nanostructures: template-confined growth and non-linear electrical transport. Small **1**, 971–975 (2005). https://doi.org/10.1002/smll.200500155
49. Liang, C., Terabe, K., Hasegawa, T., Aono, M.: Resistance switching of an individual Ag 2 S/Ag nanowire heterostructure. Nanotechnology **18**, 485202 (2007). https://doi.org/10.1088/0957-4484/18/48/485202
50. Liao, Z.-M., et al.: Resistive switching and metallic-filament formation in Ag2S nanowire transistors. Small **5**, 2377–2381 (2009). https://doi.org/10.1002/smll.200900642
51. Alissawi, N., et al.: Tuning of the ion release properties of silver nanoparticles buried under a hydrophobic polymer barrier. J. Nanoparticle Res. **14**, 928 (2012). https://doi.org/10.1007/s11051-012-0928-z
52. Li, Y., Wang, Z., Midya, R., Xia, Q., Yang, J.J.: Review of memristor devices in neuromorphic computing: materials sciences and device challenges. J. Phys. D: Appl. Phys. **51**, 503002 (2018). https://doi.org/10.1088/1361-6463/aade3f

53. Gritsenko, V.A., Perevalov, T.V., Islamov, D.R.: Electronic properties of hafnium oxide: a contribution from defects and traps. Phys. Rep. **613**, 1–20 (2016). https://doi.org/10.1016/j.physrep.2015.11.002
54. Grossi, A., Zambelli, C., Olivo, P., Crespo-Yepes, A., Martin-Martinez, J., Rodriguez, R., Nafria, M., Perez, E., Wenger, C.: Electrical characterization and modeling of 1T-1R RRAM arrays with amorphous and poly-crystalline HfO_2. Solid-State Electron. **7**, 187–193 (2016). https://doi.org/10.1016/j.sse.2016.10.025
55. Mittmann, T. et al.: Origin of ferroelectric phase in undoped HfO_2 films deposited by sputtering. Adv. Mater. Interfaces, 1900042 (2019). https://doi.org/10.1002/admi.201900042
56. Narasimhan, V.K., et al.: In situ characterization of ferroelectric HfO_2 during rapid thermal annealing. Physica Status Solidi (RRL) – Rapid Res. Lett. **15**, 2000598 (2021). https://doi.org/10.1002/pssr.202000598
57. Zhang, Y., et al.: Ion-induced damage accumulation and electron-beam-enhanced recrystallization in SrTiO3. Phys. Rev. B **72**, 094112 (2005). https://doi.org/10.1103/PhysRevB.72.094112
58. Jencic, I., Bench, M.W., Robertson, I.M., Kirk, M.A.: Electron-beam-induced crystallization of isolated amorphous regions in Si, Ge, GaP, and GaAs. J. Appl. Phys. **78**, 974–982 (1995). https://doi.org/10.1063/1.360764
59. Lulli, G., Merli, P.G., Antisari, M.V.: Solid-phase epitaxy of amorphous silicon induced by electron irradiation at room temperature. Phys. Rev. B **36**, 8038–8042 (1987). https://doi.org/10.1103/PhysRevB.36.8038
60. Kern, P., Müller, Y., Patscheider, J., Michler, J.: Electron-beam-induced topographical, chemical, and structural patterning of amorphous titanium oxide films. J. Phys. Chem. B **110**, 23660–23668 (2006). https://doi.org/10.1021/jp0642589
61. Kern, P., Widmer, R., Gasser, P., Michler, J.: Local tuning of conductivity in amorphous titanium oxide films by selective electron beam irradiation. J. Phys. Chem. C **111**, 13972–13980 (2007). https://doi.org/10.1021/jp0711803
62. Molinari, A., et al.: Configurable resistive response in BaTiO 3 ferroelectric memristors via electron beam radiation. Adv. Mater. **32**, 1907541 (2020). https://doi.org/10.1002/adma.201907541
63. Neelisetty, K.K., et al.: Electron beam effects on oxide thin films-structure and electrical property correlations. Microsc. Microanal. **25**, 592–600 (2019). https://doi.org/10.1017/S1431927619000175
64. Gronenberg, O., Carstens, N., Vahl, A., Faupel, F., Kienle, L.: In: Tiginyanu, I., Sontea, V., Railean, S. (eds.) 4th International Conference on Nanotechnologies and Biomedical Engineering. IFMBE Proceedings, pp. 71–74. Springer International Publishing, Cham (2020). https://doi.org/10.1007/978-3-030-31866-6_15
65. Vahl, A., Carstens, N., Strunskus, T., Faupel, F., Hassanien, A.: Diffusive memristive switching on the nanoscale, from individual nanoparticles towards scalable nanocomposite devices. Sci. Rep. **9** (2019). https://doi.org/10.1038/s41598-019-53720-2
66. Xia, Q., et al.: Impact of geometry on the performance of memristive nanodevices. Nanotechnology **22**, 254026 (2011). https://doi.org/10.1088/0957-4484/22/25/254026
67. Zintler, A., et al.: FIB based fabrication of an operative Pt/HfO_2/TiN device for resistive switching inside a transmission electron microscope. Ultramicroscopy **181**, 144–149 (2017). https://doi.org/10.1016/j.ultramic.2017.04.008

Open Access This chapter is licensed under the terms of the Creative Commons Attribution 4.0 International License (http://creativecommons.org/licenses/by/4.0/), which permits use, sharing, adaptation, distribution and reproduction in any medium or format, as long as you give appropriate credit to the original author(s) and the source, provide a link to the Creative Commons license and indicate if changes were made.

The images or other third party material in this chapter are included in the chapter's Creative Commons license, unless indicated otherwise in a credit line to the material. If material is not included in the chapter's Creative Commons license and your intended use is not permitted by statutory regulation or exceeds the permitted use, you will need to obtain permission directly from the copyright holder.